Exploring a cosmic-ray origin of the multiwavelength emission in M31

Alex McDaniel,[*] Tesla Jeltema,[†] and Stefano Profumo[‡]

Department of Physics, University of California, 1156 High Street, Santa Cruz, California, 95064, USA and Santa Cruz Institute for Particle Physics, 1156 High Street, Santa Cruz, California, 95064, USA

(Received 19 March 2019; published 26 July 2019)

A recent detection of spatially extended gamma-ray emission in the central region of the Andromeda galaxy (M31) has led to several possible explanations being put forth, including dark matter annihilation and millisecond pulsars. Another possibility is that the emission in M31 can be accounted for with a purely astrophysical cosmic-ray (CR) scenario. This scenario would lead to a rich multiwavelength emission that can, in turn, be used to test it. Relativistic cosmic-ray electrons (CRe) in magnetic fields produce radio emission through synchrotron radiation, while x-rays and gamma rays are produced through inverse Compton scattering. Additionally, collisions of primary cosmic-ray protons (CRp) in the interstellar medium produce charged and neutral pions that then decay into secondary CRe (detectable through radiative processes) and gamma rays. Here, we explore the viability of a CR origin for multiwavelength emission in M31, taking into consideration three scenarios: a CR scenario dominated by primary CRe, one dominated by CRp and the resulting secondary CRe and gamma rays from neutral pion decay, and a final case in which both of these components exist simultaneously. We find that the multicomponent model is the most promising, and is able to fit the multiwavelength spectrum for a variety of astrophysical parameters consistent with previous studies of M31 and of cosmic-ray physics. However, the CR power injection implied by our models exceeds the estimated CR power injection from typical astrophysical cosmic-ray sources such as supernovae.

DOI: 10.1103/PhysRevD.100.023014

I. INTRODUCTION

The study of gamma rays in galactic environments offers an intriguing probe of many physical phenomena, including cosmic-ray production and transport, star formation rates, and new physics such as dark matter. The Andromeda galaxy (M31) is particularly enticing as a target of gamma-ray studies due to its status as the nearest large spiral galaxy. M31 has been the focus of several previous gamma-ray searches [1–8]. Early observations [1–4] were only able to place upper limits until the galaxy was first detected in gamma rays using two years of Fermi-LAT data at 5.3σ significance, along with some evidence of a spatial extension at the 1.8σ confidence level [5]. It has also been observed by high-energy Cherenkov telescopes, though no detection has yet been made at energies of 1 TeV or more [9–12].

Recently, M31 was detected in gamma rays by the Fermi telescope at a significance of nearly 10σ with a detection of spatially extended emission out to ∼5 kpc at the 4σ significance level [6]. This emission resembles to some extent the well-studied Galactic Center excess (GCE) of gamma rays in the center of the Milky Way, and has led to comparisons in possible origins for the emission in the two galaxies. Proposed explanations for the GCE include signals of annihilating dark matter [13–18], an unresolved population of millisecond pulsars (MSPs) [19–21], or additional cosmic-ray sources [22–24]. Due to some similarities between both the two galaxies themselves and the observed emissions, it is natural to also consider whether these are viable explanations for the M31 detection. Although there is significant uncertainty in the dark matter density profile, the possibility of a dark matter signal in M31 has previously been studied for gamma rays [9,25,26], as well as for other wavelengths [27–33]. A brief argument is presented in the recent Fermi detection paper [6] using the relative J-factors of the Galactic Center and M31 to infer that the expected gamma-ray emission from dark matter annihilation in M31 is roughly a factor of ∼5 below the observed emission. In a recent paper [27], we studied the possibility of a dark matter origin of the M31 emission from a multiwavelength perspective. We found that when assuming a dark-matter-only interpretation using favored GCE dark matter models, such models typically require annihilation cross sections above current constraints, and have spectral shapes that are inconsistent with the M31 observations. However, this does not necessarily preclude these models contributing a subdominant component of the observed

[*]alexmcdaniel@ucsc.edu
[†]tesla@ucsc.edu
[‡]profumo@ucsc.edu

emission, with the shape of the spectrum predominantly determined by another emission source. Additionally, the dark matter particle models in that analysis that can reproduce the M31 gamma-ray emission also produce synchrotron emission that is in tension with observational radio data. There have also been efforts made to explore a millisecond pulsar explanation for the M31 gamma-ray emission [21,34]. Reference [34] studied MSPs originating from globular cluster disruption in the bulge of M31, whereas Ref. [21] considered MSPs formed *in situ*. The *in situ* model was found to fit the energetics and morphology of the excess well; however, neither study could account for the full detected emission, with each providing only $\sim 1/4$ of the M31 observation.

In light of the lack of a definitive dark matter or exclusive unresolved MSP explanation, this work focuses on the scenario in which this emission can potentially be accounted for using a conventional astrophysical interpretation of cosmic-ray-induced emissions. In order to explore this possibility, we study the multiwavelength emission in Andromeda to consider whether a cosmic-ray explanation is consistent across the spectrum. We predominantly focus on the radio and gamma-ray emission, as these regimes provide the most insight given currently available observational data. The production of cosmic rays in astrophysical systems can lead to emissions at various wavelengths, from radio to x-ray and gamma-ray [35–37]. When cosmic-ray electrons (CRe) are injected into regions containing magnetic fields, they radiate synchrotron emission at radio wavelengths, whereas through inverse Compton scattering the electrons upscatter ambient photons, such as from the CMB or starlight, to x-ray and gamma-ray energies. Gamma rays can also be produced directly through the decay of neutral pions produced in cosmic-ray proton (CRp) collisions with the interstellar medium (ISM) [38,39]. However, as first pointed out in Pshirkov *et al.* (2016) [40] and also found in the Ackermann *et al.* (2017) [6] analysis, the gamma-ray emission in M31 does not seem to be spatially correlated with neutral gas or regions of high star formation, which are typically the regions wherein CRp are expected to be produced and interact with the ISM to produce the π^0 gamma rays. The magnitudes of these fluxes depend on the components of the astrophysical environment, such as the magnetic field, the target photon radiation field, and the abundance of cosmic-ray production mechanisms. The diffusion of the relativistic cosmic rays additionally plays a significant role in the expected signal, as cosmic rays diffuse and escape the system, thus suppressing the expected flux. The mechanism by which cosmic rays are produced and accelerated has been a topic of extensive interest. For galaxies, supernovae remnants (SNRs) are considered to be the main sources of cosmic rays [41–45]. While SNRs are thought to provide the dominant contribution of cosmic rays in galaxies, other mechanisms such as pulsars and their nebulae can also provide significant contributions to the total cosmic-ray population [46–48]. The expected power injection from these cosmic-ray sources provides a benchmark to which we can compare the cosmic-ray power necessary to produce the multiwavelength emissions in M31.

This paper is organized as follows: In Sec. II we detail the relevant physical modeling, including the magnetic field, interstellar radiation field, and diffusion model, as well as the solution to the diffusion equation. In Sec. III we present the expressions for each radiative process under consideration, then in Sec. IV we present the data used in the analysis. In Sec. V we present the results of our analysis, in Sec. VI we comment on x-ray diffuse emission constraints, and, finally, we conclude in Sec. VII.

II. ASTROPHYSICAL MODEL OF ANDROMEDA

In order to calculate the secondary emission from the production of primary or secondary cosmic-ray electrons, we must first model the relevant astrophysical components of Andromeda. In particular, we require a description of the magnetic field model, which determines the synchrotron emission produced, as well as the interstellar radiation field (ISRF) that provides the target photon bath for the inverse Compton (IC) scattering. Also relevant to this analysis is a model of diffusion and radiative energy losses, since the relativistic electrons diffuse out and escape the system, while also losing energy through synchrotron emission, IC emission, Coulomb interactions, and bremsstrahlung. In the following section, we briefly describe the model adopted in this work.

A. Magnetic field

The study of radio synchrotron emission in M31 requires some knowledge of the magnetic field in our region of interest, namely within the inner few kpc. In this region, the field structure is turbulent and complex; however, estimates of the field strengths as determined by Faraday rotation measures of polarized radio emission are typically around 15 ± 3 μG for $r = 0.2$–0.4 kpc, and 19 ± 3 μG for $r = 0.8$–1.0 kpc [49,50]. At larger radii in the disk of the galaxy, the magnetic field falls off to values of roughly 5 ± 1 μG [51]. In our previous study of Andromeda, where we considered a dark matter origin of the multiwavelength emission, we selected a spatially dependent magnetic field based on these values, approximating some degree of spherical symmetry in the central region, while noting that model would not be applicable at larger radii, where a multidimensional field model would be more appropriate. In this analysis, however, we treat the magnetic field strength as one of the free parameters in our fit, and so we adopt a simplified constant magnetic field where

$$B(r) = B_\mu. \tag{1}$$

While this is helpful in that it reduces the parameters we need to fit in order to define our model, it comes at the cost of accuracy in capturing the complexity of the field or any spatial dependence. We can consider the constant field as an average over space, with a consequence of this being that we would expect the values of B_μ to be lower than the quoted central values, and at a roughly similar level to that of the disk.

B. Interstellar radiation field

Our interstellar radiation field model (ISRF) contains two components: (i) a CMB photon component and (ii) a starlight (SL) component. We have chosen to neglect the infrared (IR) component in the ISRF and instead focus only on the CMB and starlight components in order to simplify the ISRF modeling and fitting procedure, implicitly making the assumption that the starlight component will be the more significant contribution to the IC emission. For the CMB, we simply have a blackbody spectrum at $T = 2.73$ K and spatial homogeneity. Thus, we have

$$n_{\rm CMB}(\nu) = \frac{8\pi\nu^2}{c^3}\frac{1}{e^{h\nu/kT}-1}. \tag{2}$$

For the starlight component, we approximate the spectrum as a blackbody with temperature $T = 3500$ K, a choice motivated by previous analysis of the ISRF in the Milky Way demonstrating this as a good approximation for starlight spectra. We additionally include a spatial dependence based on the starlight luminosity profile of M31 [52] incorporating a bulge component of the form

$$n_{\rm bulge}(r) \propto e^{-b_n[(\frac{r}{r_b})^{1/n}-1]} \tag{3}$$

and a disk component

$$n_{\rm disk}(r) \propto e^{-\frac{r}{r_d}}. \tag{4}$$

Combining these spatial components with the blackbody spectral profile yields a starlight photon number density:

$$n_{\rm SL}(\nu, r) = N_{\rm SL}\frac{8\pi\nu^2/c^3}{e^{h\nu/kT}-1}\left[e^{-b_n[(\frac{r}{r_b})^{1/n}-1]} + \frac{e^{-\frac{r}{r_d}}}{135}\right]. \tag{5}$$

The parameters r_b, r_d, n, b_n are taken from Ref. [52], and the factor of $1/135$ in the disk component was chosen to recreate the bulge-to-disk luminosity ratio in Ref. [52]. The factor $N_{\rm SL}$ is a dimensionless normalization constant that is to be determined in the later sections as a free parameter in our fit. To get a sense for what value this parameter should be, we can consider the stellar luminosity of the inner region of M31. The stellar luminosity within a 1 kpc radius of M31 has previously been reported as $L = 10^{9.9}L_\odot$ [53,54]. We can roughly estimate the luminosity as

$$L = 4\pi r^2 c\bar{u}_{\rm SL}, \tag{6}$$

where the bar refers to a spatial average over the volume. Taking the radius to be $\sim$1 kpc, a stellar luminosity of $L = 10^{9.9}L_\odot$ corresponds to $\bar{u}_{\rm SL} \approx 5$ eV cm^{-3}, or $N_{\rm SL} \approx 5\times10^{-12}$. A reasonable, albeit somewhat large, range of values for the stellar energy density in the inner regions of galaxies is $\bar{u}_{\rm SL} \approx 1$–$10$ eV cm^{-3} [55,56], which roughly corresponds to a normalization fit range of $N_{\rm SL} \in (10^{-12}, 10^{-11})$.

C. Solution to the diffusion equation

After being injected into the system, the CRe undergo both radiative losses and diffusion. Diffusion is particularly important on shorter-distance scales, such as the few-kpc scales considered in this work, and we have demonstrated in our previous M31 paper (see Fig. 6 from Ref. [27]) that it significantly impacts the expected fluxes. The diffusion and radiative energy-loss mechanisms of the CRe are accounted for in the diffusion equation:

$$\frac{\partial}{\partial t}\frac{dn_{e^\pm}}{dE} = \nabla\left[D(E,\mathbf{r})\nabla\frac{dn_{e^\pm}}{dE}\right] + \frac{\partial}{\partial E}\left[b(E,\mathbf{r})\frac{dn_{e^\pm}}{dE}\right] + Q(E,\mathbf{r}), \tag{7}$$

where we neglect convection and reacceleration effects which can be safely ignored for energies greater than a few GeV [57,58]. Particularly in a quiescent galaxy such as M31 with its low star-formation rate [59,60], the effects of convection are expected to be less prominent than in galaxies with higher star-formation activity [61–63] such as starbursts or even the Milky Way, and thus we treat diffusion as the dominant escape term. In Eq. (7), $\partial n_e/\partial E$ is the electron/positron equilibrium spectrum with units of GeV^{-1} cm^{-3}, $D(E,\mathbf{r})$ is the diffusion coefficient, $b(E,\mathbf{r})$ is the energy-loss term, and $Q(E,\mathbf{r})$ is the CRe source term that we specify in later sections and has units of GeV^{-1} s^{-1} cm^{-3}. In the energy-loss term, we include contributions from synchrotron, IC, Coulomb, and bremsstrahlung processes, with the full expression given by

$$\begin{aligned} b(E,\mathbf{r}) &= b_{\rm IC}(E,\mathbf{r}) + b_{\rm syn}(E,\mathbf{r}) + b_{\rm Coul}(E) + b_{\rm brem}(E) \\ &= b^0_{IC}u_{\rm CMB}E^2 + b^0_{\rm IC}u_{\rm SL}(r)E^2 + b^0_{\rm syn}B^2(r)E^2 \\ &\quad + b^0_{\rm Coul}\bar{n}_e\left(1+\log\left(\frac{E/m_e}{\bar{n}_e}\right)/75\right) \\ &\quad + b^0_{\rm brem}\bar{n}_e\left(\log\left(\frac{E/m_e}{\bar{n}_e}\right)+0.36\right). \end{aligned} \tag{8}$$

The b^0 coefficients in this expression have the units GeV s^{-1} with values $b^0_{\rm syn} \simeq 0.0254$, $b^0_{\rm IC} \simeq 0.76$, $b^0_{\rm brem} \simeq 1.51$, and $b^0_{\rm Coul} \simeq 6.13$ [36,64]. The photon energy density for the

CMB is $u_{\rm CMB} = 0.25\ {\rm eV\,cm^{-3}}$, and that for the starlight photons can be computed from Eq. (5) to be $u_{\rm SL}(r) = h\nu_0^2 n_{\rm SL}(\nu_0, r)$, where ν_0 is taken to be the peak frequency. Finally, $\bar{n}_e$ in Eq. (8) refers to the average thermal electron density and is taken to be $\bar{n}_e \approx 0.01\ {\rm cm^{-3}}$ [65–69].

For the diffusion coefficient, we assume a homogeneous power law of the form

$$D(E) = D_0 E^{\delta}, \tag{9}$$

with $\delta = 1/3$ and $D_0 = 3 \times 10^{28}\ {\rm cm^2\,s^{-1}}$ [70–73]. The choices of these parameters are motivated by assuming that M31 has roughly similar diffusion properties to the Milky Way, with these values being determined by measurements of the stable (e.g., B/C) or unstable (e.g., $\mathrm{Be}^{10}/\mathrm{Be}^{9}$) secondary-to-primary ratios, and also supported by studies of the far-infrared–radio correlation in M31 and other galaxies that infer similar values [74,75]. Equation (7) can be solved analytically using the Green's function method (see, e.g., Refs. [41,64]), and in the steady-state case where the left-hand side of Eq. (7) is set to zero, the appropriate Green's function with free-escape boundary conditions is given by

$$G(r, \Delta v) = \frac{1}{\sqrt{4\pi\Delta v}} \sum_{n=-\infty}^{\infty} (-1)^n \int_0^{r_h} dr' \frac{r'}{r_n} \left(\frac{Q(E, r')}{Q(E, r)}\right) \times \left[\exp\left(-\frac{(r' - r_n)^2}{4\Delta v}\right) - \exp\left(-\frac{(r' + r_n)^2}{4\Delta v}\right)\right], \tag{10}$$

where $r_h \approx 5$ kpc is the diffusion-zone radius and the locations of the image charges used to implement the free-escape boundary condition are $r_n = (-1)^n r + 2n r_h$. The value Δv is defined as $\Delta v = v(E) - v(E')$, with

$$v(E) = \int_E^{\infty} d\tilde{E} \frac{D(\tilde{E})}{b(\tilde{E})}, \tag{11}$$

where we have approximated a spatially independent form of the energy-loss term by taking a spatial average of $u_{\rm SL}(r)$ and $B(r)$ in Eq. (8). In the above expression, E' represents the energy of the electron at the source, while E is the interaction energy. The quantity $\sqrt{\Delta v}$ has units of distance, and it represents the diffusion length scale of the particles. The final form of the electron equilibrium spectrum is then given by

$$\frac{dn_{e^\pm}}{dE}(E, r) = \frac{1}{b(E, r)} \int_E^{\infty} dE' G(r, \Delta v) Q(E, r). \tag{12}$$

Here we use the full spatially dependent form of the energy-loss expression, rather than the homogeneous form used in Eq. (11).

III. MULTIWAVELENGTH EMISSION

Once we have obtained the electron equilibrium spectrum $dn_{e^\pm}/dE$ by solving the diffusion equation, we can then proceed to calculate the emissivity j_i by integrating the electron spectrum with the power for the given radiative process, namely the synchrotron radiation and IC scattering for our purposes. This gives

$$j_i(\nu, r) = 2 \int_{m_e}^{\infty} dE\, P_i(\nu, E, r) \frac{dn_{e^\pm}}{dE}(E, r), \tag{13}$$

where the factor of 2 accounts for electrons and positrons, and P_i is the power of a radiative process i which we calculate in the following sections. From here, the flux density is given by the integral of the emissivity over volume,

$$S_i(\nu) = \frac{1}{4\pi d^2} \int dV j_i(\nu, r) \approx \frac{1}{d^2} \int dr\, r^2 j_i(\nu, r), \tag{14}$$

where d is the distance to M31, taken to be $d = 780$ kpc [76]. In this work, we make use of the publicly available RX-DMFIT tool [77] to solve the differential diffusion equation and then to perform the various secondary emission calculations. Models used in this analysis can be obtained from the authors.

A. Synchrotron power

In the presence of ambient magnetic fields, the relativistic CRe undergo synchrotron radiation, producing radio emission. The synchrotron power for a frequency ν averaged over all directions is [36,78]

$$P_{\rm syn}(\nu, E, r) = \int_0^{\pi} d\theta \frac{\sin\theta}{2} 2\pi\sqrt{3} r_0 m_e c \nu_0 \sin\theta F\left(\frac{x}{\sin\theta}\right), \tag{15}$$

where $r_0 = e^2/(m_e c^2)$ is the classical electron radius, θ is the pitch angle, and $\nu_0 = eB/(2\pi m_e c)$ is the nonrelativistic gyrofrequency. The x and F terms are defined as

$$x \equiv \frac{2\nu m_e^2}{3\nu_0 E^2}, \tag{16}$$

$$F(s) \equiv s \int_s^{\infty} d\zeta K_{5/3}(\zeta) \simeq 1.25 s^{1/3} e^{-s} [648 + s^2]^{1/12}, \tag{17}$$

where $K_{5/3}$ is the Bessel function of order 5/3.

B. Inverse Compton power

With the photon number density $n(\epsilon, r) = n_{\rm CMB}(\epsilon) + n_{\rm SL}(\epsilon, r)$ and the IC scattering cross section $\sigma(E_\gamma, \epsilon, E)$, the IC power is

$$P_{\rm IC}(E_\gamma, E, r) = cE_\gamma \int d\epsilon\, n(\epsilon, r)\sigma(E_\gamma, \epsilon, E), \quad (18)$$

where ϵ is the energy of the target photons, E is the energy of the relativistic electrons and positrons, and E_γ is the energy of the photons after scattering [note that $E_\gamma = h\nu$ for observing frequency ν in Eq. (13)]. The scattering cross section, $\sigma(E_\gamma, \epsilon, E)$, is given by the Klein-Nishina formula:

$$\sigma(E_\gamma, \epsilon, E) = \frac{3\sigma_T}{4\epsilon\gamma^2} G(q, \Gamma), \quad (19)$$

where σ_T is the Thomson cross section and $G(q, \Gamma)$ is given by [35]

$$G(q, \Gamma) = \left[2q\,\ln q + (1+2q)(1-q) + \frac{(2q)^2(1-q)}{2(1+\Gamma q)}\right], \quad (20)$$

where

$$\Gamma = \frac{4\epsilon\gamma}{m_e c^2} = \frac{4\gamma^2\epsilon}{E}, \qquad q = \frac{E_\gamma}{\Gamma(E - E_\gamma)}. \quad (21)$$

The kinematics of inverse Compton scattering set the range of q to be $1/(4\gamma^2) \le q \le 1$ [35,37,64].

C. Gamma-ray flux

In addition to gamma rays produced from IC scattering, we also consider gamma rays resulting from the decay of neutral pions produced in cosmic-ray proton collisions. When the pions are produced, they decay rapidly within a timespan of $\sim 10^{-16}$ s. The gamma rays do not experience diffusion or radiative loss effects, and thus we do not need to consider Eq. (7). Instead, for a π^0 gamma-ray source injection Q_γ (in units of GeV^{-1} cm^{-3} s^{-1}), the flux is simply given by integrating over the volume of the source [27,64,79]:

$$F_\gamma = \frac{1}{d^2} \int dr r^2 E^2 Q_\gamma(E, r). \quad (22)$$

IV. GAMMA-RAY AND RADIO DATA

The gamma-ray data points are taken from the analysis performed in Ackermann *et al.* (2017) [6], where they used 88 months of PASS 8 Fermi data collected between August 4, 2008, and December 1, 2015. Reconstructed events within an energy range of 0.1–100 GeV were considered, as well as reconstructed directions within a $14° \times 14°$ region centered at $(\alpha, \delta) = (10°.6847, 41°.2687)$. SOURCE class events were used, excluding those with zenith angle greater than 90° or rocking angle greater than 52°. The resulting detected emission found in this study was concentrated within the inner 5 kpc, motivating this as the choice of region of interest in our calculations of the gamma-ray emission resulting from IC scattering and pion decay.

Radio observations of M31 have predominantly focused on regions of large radii out to about ~16 kpc, with a particular emphasis on the star-forming 10 kpc "ring" [80–84], or alternatively on the central regions within $r \sim 1$ kpc [85,86]. For our purposes, the available data in the 1 kpc region are most useful, as they allow us to focus our analysis on the inner region and make better comparisons between the 1 kpc region of interest (ROI) for radio emission and the 5 kpc ROI for gamma-ray emission. In each of the spectral energy distributions in the following sections, the synchrotron emission is calculated with $r = 1$ kpc, while the IC and gamma-ray emissions are calculated with $r = 5$ kpc.

V. RESULTS

In our analysis, the multiwavelength emission in M31 is assumed to be due to the presence of cosmic rays. We consider here two cosmic-ray production mechanisms. The first is primary production of CRe following a power law with exponential cutoff source injection, which then radiate synchrotron and IC emission. The second source of cosmic rays we consider is primary production of cosmic-ray protons obeying a power law. The hadronic inelastic interactions of the CRp produce neutral pions that decay into gamma rays, as well as charged pions that decay into secondary CRe, which then produce synchrotron and IC emission. Finally, we consider the scenario in which both of these sources provide comparable contributions to the overall cosmic-ray abundance in what we refer to as our multicomponent model. We then examine to what extent each of these three scenarios can be responsible for the multiwavelength emission in M31. Of the three cases mentioned, the multicomponent model appears the most convincing, while the primary-only and secondary-only models do not easily reproduce the emission in M31 within the range of realistic parameter space.

A. Emission from primary cosmic-ray electrons

We now define the source term of Eq. (7) by considering the case in which the cosmic-ray population is dominated by primary electron production obeying a power law with an exponential cutoff:

$$Q_{e^\pm}(E) = N_{{\rm CR}_e} \left(\frac{E}{\rm GeV}\right)^{-\alpha_e} e^{-E/E_{\rm cut}}. \quad (23)$$

In this section, $\alpha_{\rm CR}$, $N_{{\rm CR}_e}$, and $E_{\rm cut}$ in Eq. (23) along with B_μ and $N_{\rm SL}$ are taken to be free parameters that we adjust to fit the observed radio and gamma-ray spectra. Previous studies of cosmic-ray origins can provide some guidance as to reasonable values for these parameters. For example, values of $\alpha_e \sim 2.0$–2.3 have been found to be consistent

TABLE I. Free parameters and their values in our best-fit model for a power law with an exponential cutoff primary electron source. For reference, we have included in the bottom row the experimental values for the parameters as described in the text. Reference values for the source normalization are discussed in the context of CR power output in Sec. V A 1.

α_e	$E_{\rm cut}$ (GeV)	$N_{{\rm CR}_e}$ (GeV^{-1} cm^{-3} s^{-1})	B_μ (μG)	$N_{\rm SL}$	$\chi^2_{\rm min}$/d.o.f.
2.14	514	1.1×10^{-25}	1.7	1.02×10^{-12}	3.32/7
		Observational values			
2.0–2.3	10^3–10^4	⋯	5–10	$10^{-12} - 10^{-11}$	⋯

with production of cosmic rays in supernovae (SNe), as well as suggesting $E_{\rm cut}$ values on the order of a few TeV [58,87–90]. The normalization $N_{{\rm CR}_e}$, however, is poorly constrained, and in Sec. V A 1 we compare the fit values of $N_{{\rm CR}_e}$ with the corresponding SN power output.

In Table I, we list the results for the best-fitting model and plot the spectral energy distribution (SED) in Fig. 1. Throughout this analysis, we fit the parameters by minimizing the standard χ^2 metric using a Nelder-Mead simplex algorithm [91,92] to two-decimal tolerance and employ a penalty function to enforce the fit range constraints. Additionally, the expansion, contraction, and shrink parameters are determined using a dimension-dependent implementation [93]. For the source term parameters α_e and $E_{\rm cut}$, we see a general agreement with expectations as described above, albeit with a cutoff energy somewhat lower than the TeV level. The starlight component is also suppressed to the lower end of the allowed range, with a normalization factor $N_{\rm SL} = 1.02 \times 10^{-12}$, which is a factor of ∼5 lower than the value derived in Sec. II B. We find a magnetic field value of $B_\mu = 1.7$ μG, which is relatively small in comparison to those discussed in Sec. II A. While the actual structure of the field would involve higher central values with some spatially dependent falloff, the average strength of the field over the space can be expected to take a smaller value. However, even with this in mind, the magnetic field value is particularly low and likely not representative of the field strength within the inner regions of M31, especially the inner ∼1 kpc, where the synchrotron emission is calculated. Thus, we instead seek a configuration that allows for a higher magnetic field value.

One way in which we can potentially achieve a higher magnetic field is to take into consideration the case where the radio emission is due to synchrotron radiation from cosmic-ray electrons, but the IC emission is not sufficient to recreate the Fermi observations, and remain agnostic as to the source of the gamma-ray emission. To do this, we increase the strength of the magnetic field and change $N_{{\rm CR}_e}$ to reproduce the radio emission. In Fig. 2, we show these fluxes for a few values of the magnetic field, and we list the normalization factors in Table II. In this approach, we are essentially assuming that for reasonable magnetic field values, the radio synchrotron emission in M31 can be produced predominantly by primary cosmic-ray electrons, while the source of the gamma-ray emission remains unaccounted for. In later sections, we use this approach in conjunction with comic-ray secondaries to account for the full spectrum of emission.

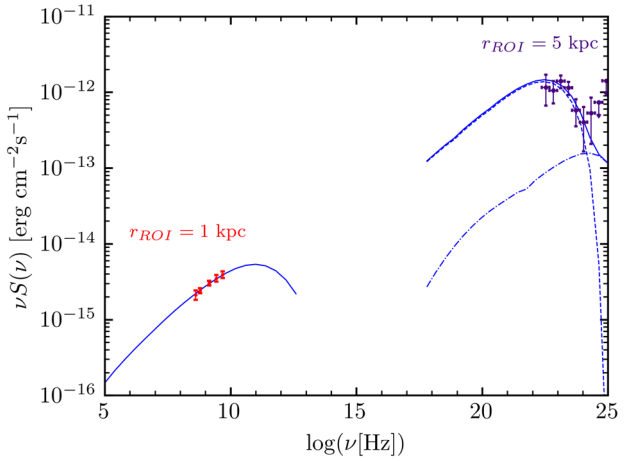

FIG. 1. Synchrotron and IC emission from primary production of CRe for the best-fit model in Table I. The dashed lines are the CMB IC contribution, the dash-dotted lines are the SL IC contribution, and the solid lines are the total emissions. Radio data are taken from Ref. [85], and gamma-ray data are taken from Ref. [6].

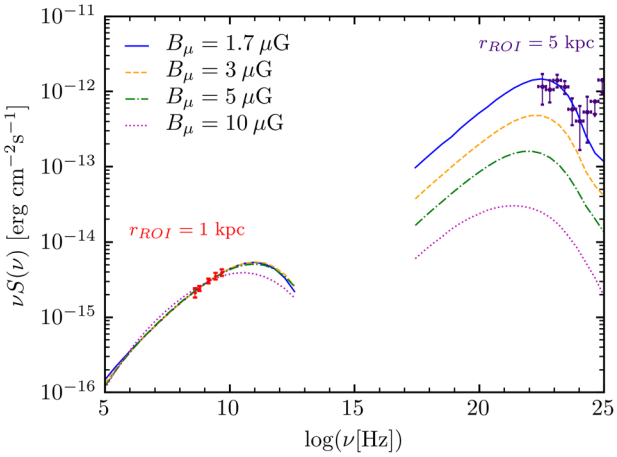

FIG. 2. Spectrum due to synchrotron and IC emission from primary CRe for various values of the magnetic field, normalized to the observed radio emission. The best-fit model is shown in green. Radio data are taken from Ref. [85], and gamma-ray data are taken from Ref. [6].

TABLE II. Normalization factors for various magnetic field strengths in the case of CRe primaries, normalized to the radio emission.

B_μ (μG)	N_{CR_e} (GeV^{-1} cm^{-3} s^{-1})
3	3.39×10^{-26}
5	1.28×10^{-26}
10	3.85×10^{-27}

1. Cosmic-ray electron power

In order to place our value for the source term normalization N_{CR_e} into a physical context, we can compare the total power output injected into cosmic-ray electrons with physical processes such as supernova explosions. The power injected into the CRe for the source term of Eq. (23) is given by

$$P_{\mathrm{CR}_e} = \int dV \int_{m_e}^{\infty} dE\, E\, Q_e(E), \tag{24}$$

where V is the diffusion volume. Meanwhile, the power injected into cosmic-ray electrons from supernovae is given by the expression

$$P_{\mathrm{SN},e} = \eta_e \Gamma E_{\mathrm{SN}} \tag{25}$$

where Γ is the supernova (SN) rate, E_{SN} is the total energy released in the SN explosion, and η_e is the efficiency of the SN energy transferred to the CRe. The SN rate can be estimated from the observed star-formation rate (SFR), which in the case of M31 has been measured to be $\sim$0.2–0.4 $\mathrm{M}_\odot\,\mathrm{yr}^{-1}$ [59,60]. Adopting a value of SFR $=$ 0.25 $\mathrm{M}_\odot\,\mathrm{yr}^{-1}$ [59], the rate is then given by [94,95]

$$\Gamma = \mathrm{SFR} \times \frac{\int_{M_{\mathrm{min}}}^{M_{\mathrm{max}}} \psi(M) dM}{\int_{0.1\ M_\odot}^{100\ M_\odot} \psi(M) M dM}. \tag{26}$$

We use the Salpeter initial mass function (IMF) [96] defined over the main-sequence mass range of 0.1–100 $M_\odot$, wherein $\psi(M) \propto M^{-2.35}$ and $\psi(M)dM$ gives the number of stars in the mass range $M + dM$. We take $M_{\mathrm{min}} = 8\ M_\odot$ and $M_{\mathrm{max}} = 40\ M_\odot$, in line with canonical CC SN parameters [94]. This yields a SN rate of 0.17 per century, and the total energy output of for one supernova explosion is $E_{\mathrm{SN}} \sim 10^{51}$ erg. While the efficiency at which energy is imparted to electrons during SN explosions is not well constrained, several estimates suggest values of $\eta_e = 10^{-5} - 10^{-3}$ [58,97]. Putting these together, we obtain a lower limit on the power injected into CRe in SN explosions to be $P_{\mathrm{SN},e} \approx 5.1 \times 10^{35}$ erg s^{-1}, and an upper limit of $P_{\mathrm{SN},e} \approx 5.1 \times 10^{37}$ erg s^{-1}. In Fig. 3, we show the power injected into CRe implied by our best-fit model while increasing the magnetic field and normalizing to the radio data (as in Fig. 2). We compare this with the estimated range of SN power output for CRe and see that the necessary normalization to fit the radio data produces a power requirement that is substantially greater than the estimated SN power budget for the lower magnetic fields, including at the best-fit value when also fitting the gamma-ray data at $B_\mu = 1.7\ \mu$G. Although the SN power calculations involve a great deal of uncertainty, it is unlikely that the uncertainty is so great that it can be reconciled with the power output implied by our parameter model. Potential other cosmic-ray acceleration mechanisms such as PWNe could also contribute to the power total; however, we can briefly demonstrate that this contribution is not enough to overcome the difference. For the case of pulsars, the relevant quantity is the spin-down luminosity, which can be expressed as

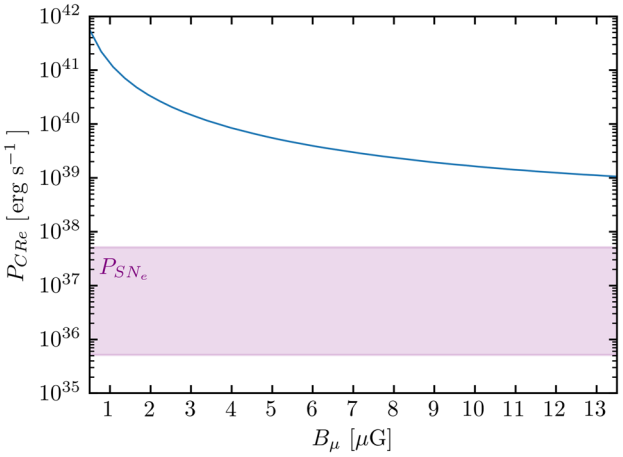

FIG. 3. Power injection into CR_e according to Eq. (24) for increasing magnetic field strength, normalized to the radio data. The purple region shows the range estimate for the electron power injection due to SNe as calculated using Eq. (25).

$$P_{\mathrm{PWN}} = \frac{\eta W_0}{t_0[1 + (\frac{t_p}{t_0})]^2}, \tag{27}$$

where η is the injection efficiency, W_0 is the pulsar energy output, t_0 is the typical pulsar decay timescale, and t_p is the pulsar lifetime [58,98–100]. If we take as fiducial values $\eta = 0.1$, $W_0 = 10^{50}$ erg, $t_0 = 1$ kyr and assume $t_p \approx t_0$, we obtain a power contribution from pulsars of

$$P_{\mathrm{PWN}} = \frac{\eta W_0}{4 t_0} \approx 8 \times 10^{37}\ \mathrm{erg\,s^{-1}}. \tag{28}$$

While this value suggests that PWNe can contribute a significant amount of the CRe power, the estimate here is not sufficient to account for the necessary CRe power of our best-fit models, and thus does not have a significant impact on the results shown in Fig. 3.

B. Emissions from cosmic rays of hadronic origin

We next consider the scenario in which the dominant contribution to the cosmic-ray population is in the form of

primary cosmic-ray protons. Inelastic interactions between the CRp and the interstellar medium produce neutral and charged pions. The neutral pions decay into gamma rays, while the charged pions decay into muons and neutrinos, which in turn decay into neutrinos and secondary CRe. This can be summarized as

$$\pi^0 \to 2\gamma,$$
$$\pi^\pm \to \mu^\pm + \nu_\mu/\bar{\nu}_\mu \to e^\pm + \nu_e/\bar{\nu}_e. \tag{29}$$

For the most common astrophysical model of the CRp distribution, we assume a simple power law:

$$n_{\mathrm{CR}_p}(E) = N_{\mathrm{CR}_p}\left(\frac{E}{\mathrm{GeV}}\right)^{-\alpha_p} \tag{30}$$

with N_{CR_p} in units of $\mathrm{GeV}^{-1}\,\mathrm{cm}^{-3}$. The resulting source terms for the gamma rays and cosmic-ray electrons have been previously calculated for this choice of CRp source distribution [39,101,102]. Following Ref. [101] for the gamma-ray source term from π^0 decay yields the expression

$$Q_\gamma(E,r) = N_{\mathrm{CR}_p} n_{\mathrm{N}}(r) c\sigma_{pp} \frac{4\xi^{2-\alpha_\gamma}}{3\alpha_\gamma}\left(\frac{m_{\pi^0}}{\mathrm{GeV}}\right)^{-\alpha_\gamma} \times \left[\left(\frac{2E_\gamma}{m_{\pi^0}}\right)^{\delta} + \left(\frac{2E_\gamma}{m_{\pi^0}}\right)^{-\delta}\right]^{-\alpha_\gamma/\delta}, \tag{31}$$

with $\alpha_\gamma = 4/3(\alpha_p - 0.5)$, and the source for $e^\pm$ from the charged pion decay is given by

$$Q_{e^\pm}(E,r) \simeq 2^6 N_{\mathrm{CR}_p} n_{\mathrm{N}}(r) c\sigma_{pp}\left(\frac{24E}{\mathrm{GeV}}\right)^{-\alpha_\gamma}, \tag{32}$$

as described in Ref. [103]. Here, $n_{\mathrm{N}}(r)$ is the nucleon number density, which we take to be proportional to the thermal electron number density with $n_{\mathrm{N}}(r) = \frac{1}{1-\frac{1}{2}X_H} n_e(r)$, where $X_H = 0.24$ is the primordial ^{4}He mass fraction. The thermal electron density $n_e(r)$ can be modeled as a beta fit of the form

$$n_e = n_{e,0}\left[1 + \left(\frac{r}{r_c}\right)^2\right]^{-\frac{3}{2}\beta}, \tag{33}$$

with $\beta = 0.49$ and $r_c = 54''$ [104] and assuming $n_{e,0} \sim 0.1\ \mathrm{cm}^{-3}$ [68,69]. The neutral pion mass is $m_{\pi^0} = 135$ GeV, ξ gives the pion multiplicity taken to be $\xi = 2$ for π^0, and $\sigma_{pp} = 32$ mbarn is the proton collision cross section. The shape parameter δ is given by $\delta = 0.14\alpha_\gamma^{-1.6} + 0.44$. For this case, when fitting to both the radio and gamma-ray data using the same free parameters as the previous section (but with E_{cut} excluded and $N_{\mathrm{CR}_e}, \alpha_e$ replaced with $N_{\mathrm{CR}_p}, \alpha_p$), we are unable to find a reasonable fit, due to the significant difference between the indices required to fit the synchrotron emission to the radio simultaneously with the π^0 decay to the gamma-ray emission. Additionally, if we ignore the contribution from π^0 gamma rays and assume that synchrotron and IC emission from secondary electrons are dominantly responsible for the observed radio and gamma-ray emission, we similarly do not find a good fit to the data.

TABLE III. Parameters and their values in our best-fit model for a power-law primary proton source.

α_p	N_{CR_p} ($\mathrm{GeV}^{-1}\,\mathrm{cm}^{-3}$)	χ^2_{min}/d.o.f.
2.66	8.89×10^{-8}	2.25/5

Instead, we determine α_p and N_{CR_p} by only fitting the π^0 gamma rays to the Fermi data, while leaving the other parameters to be determined separately. With the only contribution to the fit being from the π^0 gamma-ray contribution, we are find a best fit with $\alpha_p = 2.66$ and $N_{\mathrm{CR}_p} = 8.89 \times 10^{-8}\ \mathrm{GeV}^{-1}\,\mathrm{cm}^{-3}$, also listed in Table III. The gamma-ray spectrum is shown in Fig. 4 along with a few other values of α_p, normalized appropriately. In the selection of the remaining parameters that need to be determined (i.e., B_μ and N_{SL}), we are mainly constrained by the requirement that we be consistent with the field values in Sec. II A while not overproducing the radio emission, and that N_{SL} not result in IC emission that significantly impacts the spectrum from pion-decay gamma rays in the Fermi data energy range. In Fig. 5, we show the result of this procedure with various values for the magnetic fields, and for simplicity a single starlight normalization $N_{\mathrm{SL}} = 5 \times 10^{-12}$ in accordance with the discussion of Sec. II B. In this figure, two things are evident: first, the gamma-ray emission provides a good fit to the Fermi data; and second, the spectral index required for this fit results in a significant mismatch to the radio data regardless of normalization or field strength. The index of the CRp

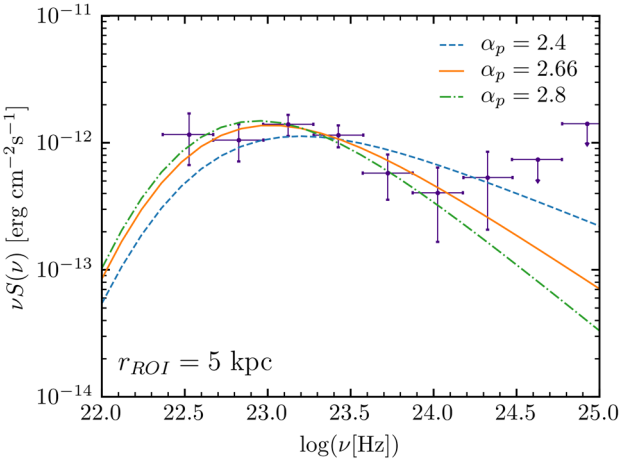

FIG. 4. Spectrum due to π^0 decay for a few values of α_p, normalized to the Fermi data from Ref. [6].

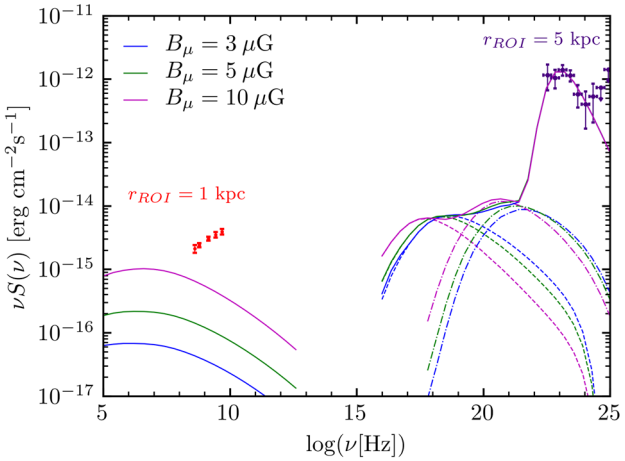

FIG. 5. Emission due to decay of $\pi^{\pm}$, π^0 into $e^{\pm}$, γ. Parameters were determined by fitting the pion-decay gamma rays to the Fermi data with only the normalization N_{CR_p} and the injection index α_p as free parameters, and for a selection of magnetic field strengths. The dashed lines are the CMB IC contribution, the dash-dotted lines are the SL IC contribution, and the solid lines are the total emissions. Radio data are taken from Ref. [85], and gamma-ray data are taken from Ref. [6].

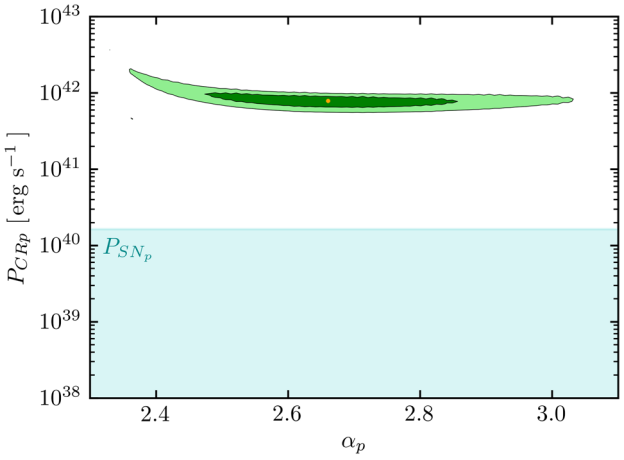

FIG. 6. 1σ and 2σ contours of power injection into CR_p according to Eq. (35), with $\mathrm{N}_{\mathrm{CR}_p}$ and α_p as free parameters and fitting only contributions from π^0 gamma rays. The light-blue region shows a portion of the range estimate for the proton power injection due to SNe as calculated using Eq. (34). The best-fit point is given by the orange dot.

distribution obtained is in agreement with other studies that suggest $\alpha_p \sim 2.5$–2.75 [105–107].

1. Cosmic-ray proton power

As we did in Sec. V A 1, we can again compare the power injected into CRp as implied by our fit parameters to the energy budget of SN-produced CRp. The power injection from SNe to CRp is of the same form as for the CRe:

$$P_{\mathrm{SN},p} = \eta_p E_{\mathrm{SN}} \Gamma_{\mathrm{SN}}, \tag{34}$$

where the only difference is in the value of the power injection efficiency, η_p. While Ref. [97] inferred a value of $\eta_p \sim 10^{-5} - 10^{-4}$, others have adopted higher values of $\eta_p \sim 10^{-3}$ [108]. Additionally, gamma-ray observations suggest that 3%–30% of the SN kinetic energy can be imparted into the cosmic-ray protons [44,109]. We therefore have quite a large range of possible values, finding $P_{\mathrm{SN},p} \approx 5.1 \times 10^{35}$ erg s^{-1} for our lower bound and $P_{\mathrm{SN},p} \approx 1.53 \times 10^{40}$ erg s^{-1} as an upper bound.

To calculate the implied CRp power from our models, we take into account the diffusive properties of the CRp source distribution n_{CR_p}. Noting that for the heavier cosmic-ray protons the radiative energy losses of Eq. (8) are unimportant, we can consider only the propagation of the CRp by diffusion. The steady-state distribution of cosmic-ray protons has a characteristic diffusion timescale of $t_D(E) \approx r_h^2/D(E)$ [36,110–113], which gives us an injection source term $n_{\mathrm{CR}_p}(E)/t_D(E)$. We then have for the power injected into CRp

$$P_{\mathrm{CR}_p} = \int dV \int_{m_p}^{\infty} dE \left(E \frac{n_{\mathrm{CR}_p}(E)}{t_D(E)} \right). \tag{35}$$

In Fig. 6, we show the contours of the implied power injected into CRp. In this case, the power determined by the fit parameters still exceeds the estimated SN power injection. This discrepancy between the SN estimates and our calculated power is not as extreme as in the primary P_{CR_e} scenario for lower magnetic fields, though for higher field values, the CRe power is just over an order of magnitude greater than the upper SN power, as opposed to the almost 2-order-of-magnitude difference for the CRp seen here.

C. Multicomponent cosmic-ray source model

In the previous sections, we were working under the assumption that the cosmic-ray source was dominated by either primary production of CRe or hadronic production of secondary CRe and π^0 gamma rays. However, another possible scenario would be one in which both of these cosmic-ray production mechanisms are incorporated. We can therefore consider a multicomponent model that includes contributions of the primary source as well as the hadronically produced sources. For the gamma-ray source term, the only contribution is from the decay of pions produced in inelastic hadronic collisions as described by Eq. (31). The electron source term for the multicomponent model is the sum of the source terms in Eqs. (23) and (32):

$$Q_{e^{\pm}}^{\mathrm{MC}}(E,r) = N_{\mathrm{CR}_e} \left(\frac{E}{\mathrm{GeV}} \right)^{-\alpha_e} e^{-E/E_{\mathrm{cut}}} + 2^6 N_{\mathrm{CR}_p} n_{\mathrm{N}}(r) c \sigma_{pp} \left(\frac{24E}{\mathrm{GeV}} \right)^{-\alpha_\gamma}, \tag{36}$$

TABLE IV. Parameters and their values in a selection of well-fitting models for the multicomponent model, along with the corresponding $\chi^2_{\rm min}$. The best-fit model parameters are given in the top row, and the corresponding SED is plotted in Fig. 7. Parameters that are held fixed in a given model are denoted with the a superscript.

α_e	α_p	$E_{\rm cut}$ (GeV)	$N_{{\rm CR}_e}$ (GeV^{-1}s^{-1} cm^{-3})	$N_{{\rm CR}_p}$ (GeV^{-1} cm^{-3})	B_μ (μG)	$N_{\rm SL}$	$\chi^2_{\rm min}$/d.o.f.
2.04	2.75	1658	1.32×10^{-26}	7.48×10^{-8}	4.8	1.10×10^{-12}	2.27/5
2.09	2.75	854	3.29×10^{-26}	5.24×10^{-8}	^{a}3	1.02×10^{-12}	2.41/6
1.92	2.71	1633	6.17×10^{-27}	7.75×10^{-8}	^{a}7	1.12×10^{-12}	2.42/6
1.71	2.67	1550	2.73×10^{-27}	7.01×10^{-8}	^{a}10	1.44×10^{-12}	2.80/6
1.57	2.70	1353	1.77×10^{-27}	7.13×10^{-8}	12.4	$^a5 \times 10^{-12}$	3.25/6

with $\alpha_\gamma = 4/3(\alpha_p - 0.5)$. The best-fit results are listed in Table IV along with a selection of parameter sets with fixed magnetic fields or fixed $N_{\rm SL}$. The SED for the best fit is shown in Fig. 7.

For the injection indices, we obtain values of $\alpha_e = 2.04$ and $\alpha_p = 2.75$, which are both within the ranges discussed in Secs. V A and V B, while the normalization factors $N_{{\rm CR}_e}$ and $N_{{\rm CR}p}$ do not deviate significantly from the values found in those sections. The cutoff energy $E_{\rm cut} = 1658$ GeV is in line with the ~TeV level used in previous cosmic-ray studies [58,87–90], but higher than in the primary-only case. The magnetic field is also higher here than in the primary-only case and is in good agreement with M31 magnetic field estimates. The similarity between the parameters of the multicomponent model and the primary-only or secondary-only models is reflected in that for the multicomponent model, each of the two components (primary and secondary) have separate regimes of dominance. That is to say, the radio is predominantly due to the primary CRe, whereas the gamma rays are mainly due to the neutral pion-decay gamma rays. This resolves the discrepancy in the model with purely hadronically produced CRe between the spectrum of radio data and the predicted synchrotron emission. In addition to the best-fit model, we also list in Table IV models in which we hold the magnetic field fixed and fit for the remaining free parameters. We do this as well where we instead hold $N_{\rm SL}$ fixed to the value discussed in Sec. II B and fit the remaining parameters. In either case, the parameter held fixed is denoted in Table IV by the a superscript. The spectra for each model in Table IV are plotted in Fig. 8. With different field strengths, we are still able to find good fits to the data, with only very slight changes to the $\chi^2_{\rm min}$. This suggests that in the multicomponent model, there is no issue with a suppressed magnetic field as in the primary-only case. Again we see that the starlight normalization is highly suppressed and the IC emission is heavily dominated by the CMB component. Since this appears to be a fairly extreme scenario for the central region of the galaxy, we try to achieve a more reasonable value by holding the normalization fixed at $N_{\rm SL} = 5 \times 10^{-12}$, as derived in Sec. II B and fitting the remaining parameters. We are still able to achieve a good fit; however, it requires a relatively higher magnetic

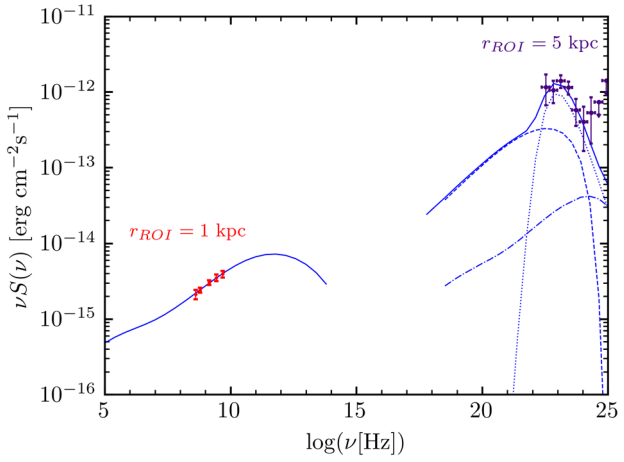

FIG. 7. SED of the best-fitting multicomponent CR model, including contributions from primary CRe, as well as secondary CRe and gamma rays of hadronic origin. Fit parameters are listed in the top row of Table IV. The dashed lines are the IC CMB contribution, the dash-dotted lines are the IC SL contribution, the dotted lines are the π^0 gamma rays, and the solid lines are the total emissions. Radio data are taken from Ref. [85], and gamma-ray data are taken from Ref. [6].

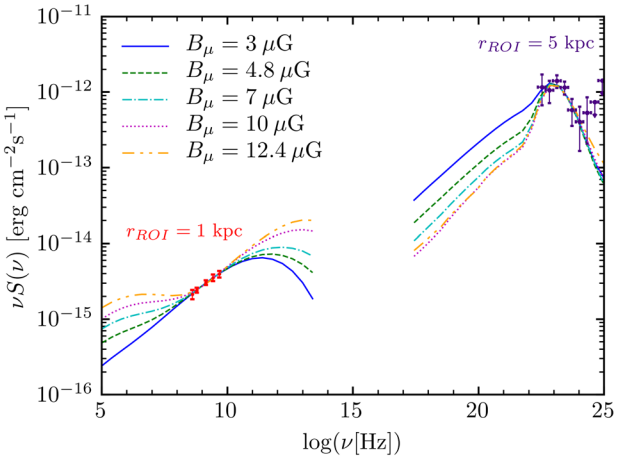

FIG. 8. SED of the multicomponent CR model for each of the parameter sets in Table IV. Radio data are taken from Ref. [85], and gamma-ray data are taken from Ref. [6].

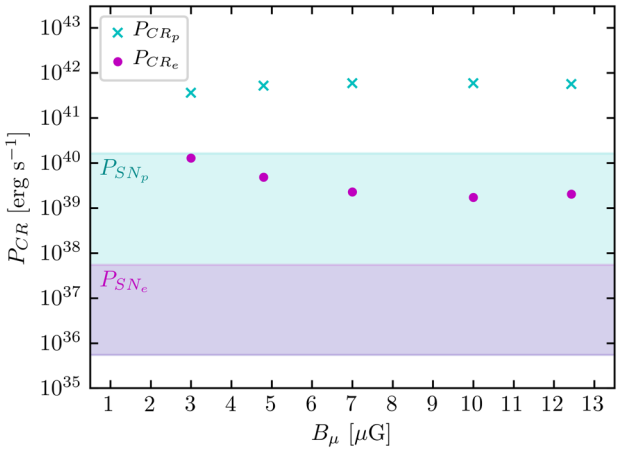

FIG. 9. Power injection into CRe and CRp for each of the models in Table IV, plotted against magnetic field. Note that the region of SN power injection into CRp (cyan) fully overlaps the region of SN power injection into CRe (magenta).

field of $B_\mu = 12.4$ μG in order to suppress the stellar IC component, as well as a low injection index of $\alpha_e = 1.57$.

We once again compare the power injection into CRe and CRp implied by the parameters of our fit with the estimated SN-injected power. Noting that the source term parameters for the CRe and CRp do not deviate significantly from the values found in Secs. V A and V B, similar results in this comparison can be expected here. In fact, that is essentially what we see in Fig. 9, wherein we show the implied CR power from our models for the various magnetic field values compared with the SN power injection estimates of Secs. V A 1 and V B 1. We see that the implied CRe power injection decreases for models with a higher magnetic field (cf. Fig. 3), while the CRp injection remains relatively constant with some slight increase due to suppression of the primary CRe-induced IC emission. However, neither are within their respective ranges for the SN source power. Although there is a discrepancy between the implied power injection of our cosmic-ray parameter sets and the estimated supernova contribution, the great deal of uncertainty in the SN power estimates makes it difficult to make concrete statements on the viability of these models on this basis alone.

VI. DIFFUSE X-RAY EMISSION IN M31

While the focus of this analysis has been on the radio and gamma-ray emission, x-ray emission in M31 provides another potential avenue to study. However, several observations of the x-ray emission in the bulge of M31 have detected the presence of an unresolved diffuse component, using data from ROSAT [114,115], XMM-Newton [116], and CHANDRA [117]. In each of these studies, diffuse x-ray flux in the inner ~1 kpc of M31 is observed at a flux level of roughly ~ 3–5×10^{-12} erg cm^{-2} s^{-1}, and can likely be attributed to the presence of thermal hot gas and unresolved x-ray point sources. We note that this observed x-ray emission within 1 kpc has a higher flux than the x rays produced in any of our cosmic-ray models from the previous sections, even despite the computed x-ray emission being within a 5 kpc radius. We thus conclude that for these cosmic-ray models and our astrophysical setup, the x-ray emission in M31 does not provide particularly useful information due to the bright diffuse emission in the bulge of M31 being considerably brighter than what we would obtain in our models.

VII. CONCLUSION

We have examined the possibility of a cosmic-ray origin for the multiwavelength emission in the Andromeda galaxy, specifically addressing the origin of the recently detected extended gamma-ray emission. We considered three models for the production of cosmic rays. First, we considered a primary injection of CRe obeying a power law with an exponential cutoff, then considered the production of secondary CRe and gamma rays produced from interactions of a power-law distribution of primary CRp. Finally, we looked at a multicomponent model that incorporates both of these cosmic-ray sources. We then fit the synchrotron and IC fluxes arising due to the presence of the primary and secondary CRe, as well as the gamma-ray emission from neutral pion decay, to available radio data and a recent Fermi gamma-ray detection in M31.

For the primary CRe scenario, we find best-fit parameters for the injection spectrum $\alpha_e = 2.14$ and cutoff energy $E_{\rm cut} = 514$ GeV. The injection index is consistent with expected values for CRe sources such as SNR. The cutoff energy is slightly lower than expected, however not wholly inconsistent with expected values on the order of TeV. The magnetic field value of $B_\mu = 1.7$ μG and the starlight normalization are both suppressed in the fit. We also considered higher magnetic fields and renormalized the synchrotron emission to match the radio data. This suppresses the IC gamma-ray emission, requiring that we account for the Fermi data separately, which was done in the multicomponent model. We then compared the power injection into CRe implied by our model with the expected range of power injection due to SNe. We saw that even by increasing the magnetic field in order to lower the normalization constant $N_{\rm CR_e}$, the power injection implied by our models was well above the expected output from astrophysical sources such as PWNe and SNe.

In the case where we considered contributions from only secondary cosmic rays of hadronic origin, we were unable to find a good fit to both the radio and gamma-ray data simultaneously. Rather, we assumed that the gamma rays were purely from the neutral pion decay and found a CRp distribution index of $\alpha_p = 2.66$, consistent with previous results for π^0 gamma-ray studies, along with a CRp distribution coefficient of $N_{\rm CR_p} = 8.89 \times 10^{-8}$ GeV^{-1} cm^{-3}. With this arrangement, we then manually selected the

magnetic field and starlight energy density, and found that for a variety of field strengths the calculated flux remains below the radio data, and even for a higher selected value of $N_{\rm SL} = 5 \times 10^{-12}$, there was no conflict between the IC emission and the gamma-ray data. We again compared the power injection into CRp from SNe with the implied power output of our models, and found that the CRp injection is also greater than the estimated SN output.

Finally, we consider a combined "multicomponent model" that incorporates the contributions from both the primary CRe as well as the secondary CRe of hadronic origin. Although here the power budget concerns remained due to minimal variation in the best-fit normalization constants, this scenario gives the best overall fit to the data, while still providing similar parameter values as in the primary-only and secondary-only cases. We found the best-fit $\alpha_e = 2.04$ and $\alpha_p = 2.75$, both similar to the values discussed in Secs. V A and V B, respectively, while the best-fit magnetic field was found to be $B_\mu = 4.8\ \mu$G, and $E_{\rm cut}$ was 1658 GeV. Additionally, the multicomponent model offers a large degree of flexibility in the parameter choices, as evidenced by good fits for a range of multiple magnetic field values and $E_{\rm cut}$ on the order of a few TeV, as well as for higher $N_{\rm SL}$ values in accordance with the observed stellar luminosity in the central region of M31. In our final power comparison, we saw similar results as in the primary-only and secondary-only scenarios. That is, both the implied CRe and CRp power in our models were greater than the estimated power output from astrophysical sources, and this held at a wide range of magnetic field values. This suggests that although the spectra can be fit well with a multicomponent model, the input power needed for the cosmic-ray sources is consistently more than an order of magnitude above what is expected from supernovae as galactic cosmic-ray accelerators. Furthermore, as mentioned in the Introduction and discussed more thoroughly in the original detection paper [6] along with earlier and subsequent Fermi M31 studies [21,34,40], the gamma-ray emission does not appear to correlate with star formation or gas-rich regions. CRp produced at larger radii that then diffuse into the emission region may contribute to the observed signal, although this does not address the lack of gas for the CRp to interact with in the interior regions of the galaxy. Another possibility is that the CRp are remnants from a previous period of higher star formation. However, the stellar population of the bulge is dominated by stars with ages $\gtrsim$4–12 Gyr [118–120], compared to a CRp escape time of $\sim$10–100 Myr, which suggests that the majority of CRp would have likely left the system in the time since this higher star-formation activity in M31. This morphological point along with the power discrepancy combine to disfavour a purely CR explanation, particularly one that relies on π^0 gamma rays from CRp to explain the observed gamma-ray emission.

ACKNOWLEDGMENTS

This study is based on work supported by the National Science Foundation under Grant No. 1517545. A. M. is supported by a Department of Education GAANN fellowship. S. P. is partly supported by the U.S. Department of Energy, Grant No. DE-SC0010107.

[1] C. E. Fichtel, R. C. Hartman, D. A. Kniffen, D. J. Thompson, G. F. Bignami, H. Ögelman, M. E. Özel, and T. Tümer, High-energy gamma-ray results from the second small astronomy satellite. Astrophys. J. **198**, 163 (1975).

[2] A. M. T. Pollock, G. F. Bignami, W. Hermsen, G. Kanbach, G. G. Lichti, J. L. Masnou, B. N. Swanenburg, and R. D. Wills, Search for gamma-radiation from extragalactic objects using a likelihood method, Astron. Astrophys. **94**, 116 (1981).

[3] P. Sreekumar, D. L. Bertsch, B. L. Dingus, J. A. Esposito, C. E. Fichtel, R. C. Hartman, S. D. Hunter, G. Kanbach, D. A. Kniffen, Y. C. Lin, J. R. Mattox, H. A. Mayer-Hasselwander, P. F. Michelson, C. von Montigny, P. L. Nolan, E. J. Schneid, and D. J. Thompson, A study of M31, M87, NGC 253, and M82 in high-energy gamma rays, Astrophys. J. **426**, 105 (1994).

[4] J. J. Blom, T. A. D. Paglione, and Alberto Carramiñana, Diffuse gamma-ray emission from starburst Galaxies and M31, Astrophys. J. **516**, 744 (1999).

[5] A. A. Abdo *et al.*, Fermi large area telescope observations of local group galaxies: Detection of M31 and search for M33, Astron. Astrophys. **523**, L2 (2010).

[6] M. Ackermann *et al.*, Observations of M31 and M33 with the Fermi large area telescope: A galactic center excess in Andromeda?, Astrophys. J. **836**, 208 (2017).

[7] C. Karwin, S. Murgia, S. Campbell, and I. Moskalenko, Fermi-LAT observations of gamma-ray emission towards the outer halo of M31, arXiv:1903.10533.

[8] L. Feng, Z. Li, M. Su, .-H. T. Tam, and Y. Chen, Searching for GeV gamma-ray emission from the bulge of M31, Res. Astron. Astrophys. **19**, 046 (2019).

[9] A. Albert, Search for dark matter gamma-ray emission from the Andromeda galaxy with the high-altitude water Cherenkov observatory, J. Cosmol. Astropart. Phys. 06 (2018) 043.

[10] R. Bird (VERITAS Collaboration), VERITAS observations of M31 (the Andromeda galaxy), Proc. Sci. (ICRC2015) (**2016**) 851.

[11] F. A. Aharonian *et al.*, Search for TeV gamma ray emission from the Andromeda galaxy, Astron. Astrophys. **400**, 153 (2003).
[12] R. Rubenzahl, S. BenZvi, and J. Wood (HAWC Collaboration), Limits on the emission of gamma rays from M31 (the Andromeda galaxy) with HAWC, Int. Cosmic Ray Conf. **301**, 594 (2017).
[13] K. N. Abazajian, N. Canac, S. Horiuchi, and M. Kaplinghat, Astrophysical and dark matter interpretations of extended gamma-ray emission from the Galactic Center, Phys. Rev. D **90**, 023526 (2014).
[14] F. Calore, I. Cholis, C. McCabe, and C. Weniger, A tale of tails: Dark matter interpretations of the Fermi GeV excess in light of background model systematics, Phys. Rev. D **91**, 063003 (2015).
[15] T. Daylan, D. P. Finkbeiner, D. Hooper, T. Linden, S. K. N. Portillo, N. L. Rodd, and T. R. Slatyer, The characterization of the gamma-ray signal from the central Milky Way: A case for annihilating dark matter, Phys. Dark Universe **12**, 1 (2016).
[16] C. Gordon and O. Macías, Dark matter and pulsar model constraints from Galactic Center Fermi-LAT gamma-ray observations, Phys. Rev. D **88**, 083521 (2013).
[17] D. Hooper and L. Goodenough, Dark matter annihilation in the Galactic center as seen by the Fermi Gamma Ray space telescope, Phys. Lett. B **697**, 412 (2011).
[18] L. Goodenough and D. Hooper, Possible evidence for dark matter annihilation in the inner Milky Way from the Fermi gamma ray space telescope, arXiv:0910.2998.
[19] R. Bartels, S. Krishnamurthy, and C. Weniger, Strong Support for the Millisecond Pulsar Origin of the Galactic Center GeV Excess, Phys. Rev. Lett. **116**, 051102 (2016).
[20] T. D. Brandt and B. Kocsis, Disrupted globular clusters can explain the Galactic Center gamma-ray excess, Astrophys. J. **812**, 15 (2015).
[21] C. Eckner, X. Hou, P. D. Serpico, M. Winter, G. Zaharijas, P. Martin, M. di Mauro, N. Mirabal, J. Petrovic, T. Prodanovic, and J. Vandenbroucke, Millisecond pulsar origin of the Galactic Center excess and extended gamma-ray emission from Andromeda: A closer look, Astrophys. J. **862**, 79 (2018).
[22] E. Carlson, S. Profumo, and T. Linden, Cosmic-Ray Injection from Star-Forming Regions, Phys. Rev. Lett. **117**, 111101 (2016).
[23] D. Gaggero, M. Taoso, A. Urbano, M. Valli, and P. Ullio, Towards a realistic astrophysical interpretation of the gamma-ray Galactic Center excess, J. Cosmol. Astropart. Phys. 12 (2015) 056.
[24] I. Cholis, C. Evoli, F. Calore, T. Linden, C. Weniger, and D. Hooper, The Galactic Center GeV excess from a series of leptonic cosmic-ray outbursts, J. Cosmol. Astropart. Phys. 12 (2015) 005.
[25] N. Fornengo, L. Pieri, and S. Scopel, Neutralino annihilation into γ rays in the Milky Way and in external galaxies, Phys. Rev. D **70**, 103529 (2004).
[26] Z. Li, X. Huang, Q. Yuan, and Y. Xu, Constraints on the dark matter annihilation from Fermi-LAT observation of M31, J. Cosmol. Astropart. Phys. 12 (2016) 028.
[27] A. McDaniel, T. Jeltema, and S. Profumo, Multiwavelength analysis of annihilating dark matter as the origin of the gamma-ray emission from M31, Phys. Rev. D **97**, 103021 (2018).
[28] A. E. Egorov and E. Pierpaoli, Constraints on dark matter annihilation by radio observations of M31, Phys. Rev. D **88**, 023504 (2013).
[29] G. Beck and S. Colafrancesco, A multi-frequency analysis of possible dark matter contributions to M31 gamma-ray emissions, J. Cosmol. Astropart. Phys. 10 (2017) 007.
[30] M. H. Chan, Revisiting the constraints on annihilating dark matter by the radio observational data of M31, Phys. Rev. D **94**, 023507 (2016).
[31] K. C. Y. Ng, B. M. Roach, K. Perez, J. F. Beacom, S. Horiuchi, R. Krivonos, and D. R. Wik, New constraints on sterile neutrino dark matter from *NuSTAR* M31 observations, Phys. Rev. D **99**, 083005 (2019).
[32] A. Boyarsky, D. Iakubovskyi, O. Ruchayskiy, and V. Savchenko, Constraints on decaying dark matter from XMM-Newton observations of M31, Mon. Not. R. Astron. Soc. **387**, 1361 (2008).
[33] C. R. Watson, Z. Li, and N. K. Polley, Constraining sterile neutrino warm dark matter with Chandra observations of the Andromeda galaxy, J. Cosmol. Astropart. Phys. 03 (2012) 018.
[34] G. Fragione, F. Antonini, and O. Y. Gnedin, Millisecond pulsars and the gamma-ray excess in Andromeda, Astrophys. J. Lett. **871**, L8 (2019).
[35] G. R. Blumenthal and R. J. Gould, Bremsstrahlung, synchrotron radiation, and Compton scattering of high-energy electrons traversing dilute gases, Rev. Mod. Phys. **42**, 237 (1970).
[36] M. S. Longair, *High Energy Astrophysics*, 3rd ed. (Cambridge University Press, New York, 2011).
[37] G. B. Rybicki and A. P. Lightman, *Radiative Processes in Astrophysics* (Wiley, New York, 1979).
[38] C. D. Dermer, Secondary production of neutral pi-mesons and the diffuse galactic gamma radiation, Astron. Astrophys. **157**, 223 (1986).
[39] K. Mannheim and R. Schlickeiser, Interactions of cosmic ray nuclei, Astron. Astrophys. **286**, 983 (1994).
[40] M. S. Pshirkov, V. V. Vasiliev, and K. A. Postnov, Evidence of Fermi bubbles around M31, Mon. Not. R. Astron. Soc. **459**, L76 (2016).
[41] V. L. Ginzburg and S. I. Syrovatskii, *The Origin of Cosmic Rays* (Pergamon Press, Oxford, 1964).
[42] E. G. Berezhko, Origin of Galactic cosmic rays from supernova remnants, Nucl. Phys. B, Proc. Suppl. **256**, 23 (2014).
[43] A. R. Bell, Cosmic ray acceleration, Astropart. Phys. **43**, 56 (2013), Seeing the high-energy Universe with the Cherenkov telescope array: The science explored with the CTA.
[44] D. J. Thompson, L. Baldini, and Y. Uchiyama, Cosmic ray studies with the Fermi gamma-ray space telescope large area telescope, Astropart. Phys. **39–40**, 22 (2012).
[45] L. O.C. Drury, Origin of cosmic rays, Astropart. Phys. **39–40**, 52 (2012).
[46] F. A. Aharonian, A. M. Atoyan, and H. J. Voelk, High energy electrons and positrons in cosmic rays as an indicator of the existence of a nearby cosmic Tevatron, Astron. Astrophys. **294**, L41 (1995).

[47] L. Gendelev, S. Profumo, and M. Dormody, The contribution of Fermi gamma-ray pulsars to the local flux of cosmic-ray electrons and positrons, J. Cosmol. Astropart. Phys. 02 (2010) 016.
[48] D. Hooper, P. Blasi, and P. D. Serpico, Pulsars as the sources of high energy cosmic ray positrons, J. Cosmol. Astropart. Phys. 01 (2009) 025.
[49] P. Hoernes, R. Beck, and E. M. Berkhuijsen, Properties of synchrotron emission and magnetic fields in the central region of M31, in *The Central Regions of the Galaxy and Galaxies, Volume 184 of IAU Symposium*, edited by Y. Sofue (1998), p. 351.
[50] R. Gießübel and R. Beck, The magnetic field structure of the central region in M31, Astron. Astrophys. **571**, A61 (2014).
[51] A. Fletcher, E. M. Berkhuijsen, R. Beck, and A. Shukurov, The magnetic field of M31 from multi-wavelength radio polarization observations, Astron. Astrophys. **414**, 53 (2004).
[52] S. Courteau, L. M. Widrow, M. McDonald, P. Guhathakurta, K. M. Gilbert, Y. Zhu, R. L. Beaton, and S. R. Majewski, The luminosity profile and structural parameters of the Andromeda galaxy, Astrophys. J. **739**, 20 (2011).
[53] B. Groves, O. Krause, K. Sandstrom, A. Schmiedeke, A. Leroy, H. Linz, M. Kapala, H.-W. Rix, E. Schinnerer, F. Tabatabaei, F. Walter, and E. da Cunha, The heating of dust by old stellar populations in the bulge of M31, Mon. Not. R. Astron. Soc. **426**, 892 (2012).
[54] B. T. Draine, G. Aniano, O. Krause, B. Groves, K. Sandstrom, R. Braun, A. Leroy, U. Klaas, H. Linz, H.-W. Rix, E. Schinnerer, A. Schmiedeke, and F. Walter, Andromeda's dust, Astrophys. J. **780**, 172 (2014).
[55] S. Profumo and P. Ullio, Multi-wavelength searches for particle dark matter, arXiv:1001.4086.
[56] T. A. Porter, I. V. Moskalenko, A. W. Strong, E. Orlando, and L. Bouchet, Inverse Compton origin of the hard x-ray and soft gamma-ray emission from the Galactic ridge, Astrophys. J. **682**, 400 (2008).
[57] T. Delahaye, R. Lineros, F. Donato, N. Fornengo, J. Lavalle, P. Salati, and R. Taillet, Galactic secondary positron flux at the Earth, Astron. Astrophys. **501**, 821 (2009).
[58] T. Delahaye, J. Lavalle, R. Lineros, F. Donato, and N. Fornengo, Galactic electrons and positrons at the Earth: New estimate of the primary and secondary fluxes, Astron. Astrophys. **524**, A51 (2010).
[59] G. P. Ford, W. K. Gear, M. W. L. Smith, S. A. Eales, M. Baes, G. J. Bendo, M. Boquien, A. Boselli, A. R. Cooray, and I. De Looze, Herschel exploitation of local galaxy Andromeda (HELGA): III. The star formation law in M31, Astrophys. J. **769**, 55 (2013).
[60] S. Rahmani, S. Lianou, and P. Barmby, Star formation laws in the Andromeda Galaxy: Gas, stars, metals and the surface density of star formation, Mon. Not. R. Astron. Soc. **456**, 4128 (2016).
[61] A. McCormick, S. Veilleux, and D. S. N. Rupke, Dusty winds: Extraplanar polycyclic aromatic hydrocarbon features of nearby galaxies, Astrophys. J. **774**, 126 (2013).
[62] B. C. Lacki, T. A. Thompson, and E. Quataert, The physics of the far-infrared-radio correlation: I. Calorimetry, conspiracy, and implications, Astrophys. J. **717**, 1 (2010).
[63] S. Veilleux, G. Cecil, and J. Bland-Hawthorn, Galactic winds, Annu. Rev. Astron. Astrophys. **43**, 769 (2005).
[64] S. Colafrancesco, S. Profumo, and P. Ullio, Multi-frequency analysis of neutralino dark matter annihilations in the Coma cluster, Astron. Astrophys. **455**, 21 (2006).
[65] B. M. Gaensler, G. J. Madsen, S. Chatterjee, and S. A. Mao, The vertical structure of warm ionised gas in the Milky Way, Pub. Astron. Soc. Aust. **25**, 184 (2008).
[66] E. M. Berkhuijsen, D. Mitra, and P. Mueller, Filling factors and scale heights of the diffuse ionized gas in the Milky Way, Astron. Nachr. **327**, 82 (2006).
[67] E. M. Berkhuijsen and P. Müller, Densities and filling factors of the diffuse ionized gas in the solar neighbourhood, Astron. Astrophys. **490**, 179 (2008).
[68] D. Caprioli, Understanding hadronic gamma-ray emission from supernova remnants, J. Cosmol. Astropart. Phys. 05 (2011) 026.
[69] D. Caprioli, E. Amato, and P. Blasi, The contribution of supernova remnants to the galactic cosmic ray spectrum, Astropart. Phys. **33**, 160 (2010).
[70] A. W. Strong, I. V. Moskalenko, and V. S. Ptuskin, Cosmic-ray propagation and interactions in the Galaxy, Annu. Rev. Nucl. Part. Sci. **57**, 285 (2007).
[71] A. E. Vladimirov, G. Jóhannesson, I. V. Moskalenko, and T. A. Porter, Testing the origin of high-energy cosmic rays, Astrophys. J. **752**, 68 (2012).
[72] E. A. Baltz and J. Edsjö, Positron propagation and fluxes from neutralino annihilation in the halo, Phys. Rev. D **59**, 023511 (1998).
[73] W. R. Webber, M. A. Lee, and M. Gupta, Propagation of cosmic-ray nuclei in a diffusing galaxy with convective halo and thin matter disk, Astrophys. J. **390**, 96 (1992).
[74] E. M. Berkhuijsen, R. Beck, and F. S. Tabatabaei, How cosmic ray electron propagation affects radio-far-infrared correlations in M31 and M33, Mon. Not. R. Astron. Soc. **435**, 1598 (2013).
[75] E. J. Murphy, G. Helou, R. Braun, J. D. P. Kenney, L. Armus, D. Calzetti, B. T. Draine, R. C. Kennicutt, Jr., H. Roussel, F. Walter, G. J. Bendo, B. Buckalew, D. A. Dale, C. W. Engelbracht, J. D. T. Smith, and M. D. Thornley, The effect of star formation on the far-infrared-radio correlation within galaxies, Astrophys. J. **651**, L111 (2006).
[76] K. Z. Stanek and P. M. Garnavich, Distance to M31 with the Hubble Space Telescope and HIPPARCOS red clump stars, Astrophys. J. Lett. **503**, L131 (1998).
[77] A. McDaniel, T. Jeltema, S. Profumo, and E. Storm, Multiwavelength analysis of dark matter annihilation and RX-DMFIT, J. Cosmol. Astropart. Phys. 09 (2017) 027.
[78] E. Storm, T. E. Jeltema, M. Splettstoesser, and S. Profumo, Synchrotron emission from dark matter annihilation: Predictions for constraints from non-detections of galaxy clusters with new radio surveys, Astrophys. J. **839**, 33 (2017).
[79] M. Regis and P. Ullio, Multiwavelength signals of dark matter annihilations at the Galactic Center, Phys. Rev. D **78**, 043505 (2008).
[80] E. M. Berkhuijsen, R. Beck, and P. Hoernes, The polarized disk in M31 at $\lambda 6$ cm, Astron. Astrophys. **398**, 937 (2003).

[81] R. Gießübel, G. Heald, R. Beck, and T. G. Arshakian, Polarized synchrotron radiation from the Andromeda galaxy M31 and background sources at 350 MHz, Astron. Astrophys. **559**, A27 (2013).
[82] R. Beck, E. M. Berkhuijsen, and R. Wielebinski, Distribution of polarised radio emission in M31, Nature (London) **283**, 272 (1980).
[83] R. Beck, E. M. Berkhuijsen, and P. Hoernes, A deep λ 20 cm radio continuum survey of M31, Astron. Astrophys. Suppl. Ser. **129**, 329 (1998).
[84] R. Beck and R. Graeve, The distribution of thermal and nonthermal radio continuum emission of M31, Astron. Astrophys. **105**, 192 (1982).
[85] R. A. M. Walterbos and R. Graeve, Radio continuum emission from the nuclear region of M31 evidence for a nuclear radio spiral, Astron. Astrophys. **150**, L1 (1985).
[86] E. M. Berkhuijsen, R. Wielebinski, and R. Beck, A radio continuum survey of M31 at 4850 MHz: I. Observations: List of sources, Astron. Astrophys. **117**, 141 (1983).
[87] M. Di Mauro, F. Donato, N. Fornengo, R. Lineros, and A. Vittino, Interpretation of AMS-02 electrons and positrons data, J. Cosmol. Astropart. Phys. 04 (2014) 006.
[88] S. Manconi, M. Di Mauro, and F. Donato, Dipole anisotropy in cosmic electrons and positrons: Inspection on local sources, J. Cosmol. Astropart. Phys. 01 (2017) 006.
[89] K. Fang, B.-B. Wang, X.-J. Bi, S.-J. Lin, and P.-F. Yin, Perspective on the cosmic-ray electron spectrum above TeV, Astrophys. J. **836**, 172 (2017).
[90] G. Di Bernardo, C. Evoli, D. Gaggero, D. Grasso, and L. Maccione, Cosmic ray electrons, positrons and the synchrotron emission of the Galaxy: Consistent analysis and implications, J. Cosmol. Astropart. Phys. 03 (2013) 036.
[91] J. A. Nelder and R. Mead, A simplex method for function minimization, Comput. J. **7**, 308 (1965).
[92] W. H. Press, *Numerical Recipes 3rd Edition: The Art of Scientific Computing* (Cambridge University Press, Cambridge, England, 2007).
[93] F. Gao and L. Han, Implementing the Nelder-Mead simplex algorithm with adaptive parameters, Comput. Optim. Appl. **51**, 259 (2012).
[94] S. Horiuchi, J. F. Beacom, C. S. Kochanek, J. L. Prieto, K. Z. Stanek, and T. A. Thompson, The cosmic core-collapse supernova rate does not match the massive-star formation rate, Astrophys. J. **738**, 154 (2011).
[95] M. T. Botticella, S. J. Smartt, R. C. Kennicutt, E. Cappellaro, M. Sereno, and J. C. Lee, A comparison between star formation rate diagnostics and rate of core collapse supernovae within 11 Mpc, Astron. Astrophys. **537**, A132 (2012).
[96] E. E. Salpeter, The luminosity function and stellar evolution, Astrophys. J. **121**, 161 (1955).
[97] V. Tatischeff, Radio emission and nonlinear diffusive shock acceleration of cosmic rays in the supernova SN 1993J, Astron. Astrophys. **499**, 191 (2009).
[98] D. Malyshev, I. Cholis, and J. Gelfand, Pulsars versus dark matter interpretation of ATIC/PAMELA, Phys. Rev. D **80**, 063005 (2009).
[99] S. Della Torre, M. Gervasi, P. G. Rancoita, D. Rozza, and A. Treves, Pulsar wind nebulae as a source of the observed electron and positron excess at high energy: The case of Vela-X, J. High Energy Astrophys. 08 (**2015**) 027.
[100] T. Linden and S. Profumo, Probing the pulsar origin of the anomalous positron fraction with AMS-02 and atmospheric Cherenkov telescopes, Astrophys. J. **772**, 18 (2013).
[101] C. Pfrommer and T. A. Enßlin, Constraining the population of cosmic ray protons in cooling flow clusters with γ-ray and radio observations: Are radio mini-halos of hadronic origin? Astron. Astrophys. **413**, 17 (2004).
[102] R. Schlickeiser, *Cosmic Ray Astrophysics* (Springer, Berlin, 2002).
[103] K. Dolag and T. A. Enßlin, Radio halos of galaxy clusters from hadronic secondary electron injection in realistic magnetic field configurations, Astron. Astrophys. **362**, 151 (2000).
[104] J. Liu, Q. D. Wang, Z. Li, and J. R. Peterson, X-ray spectroscopy of the hot gas in the M31 bulge, Mon. Not. R. Astron. Soc. **404**, 1879 (2010).
[105] P. Blasi and E. Amato, Diffusive propagation of cosmic rays from supernova remnants in the Galaxy: I. Spectrum and chemical composition, J. Cosmol. Astropart. Phys. 01 (2012) 010.
[106] C.-Y. Huang, Gamma-ray energy spectra through decays of neutral pions produced in proton-proton interactions, Int. Cosmic Ray Conf. **4**, 2297 (2003).
[107] T. A. D. Paglione, A. P. Marscher, J. M. Jackson, and D. L. Bertsch, Diffuse gamma-ray emission from the Starburst galaxy NGC 253, Astrophys. J. **460**, 295 (1996).
[108] G. Cassam-Chenaı, J. P. Hughes, J. Ballet, and A. Decourchelle, The blast wave of Tycho's supernova remnant, Astrophys. J. **665**, 315 (2007).
[109] M. Ackermann *et al.*, Detection of the characteristic pion-decay signature in supernova remnants, Science **339**, 807 (2013).
[110] A. M. Taylor, S. Gabici, and F. Aharonian, Galactic halo origin of the neutrinos detected by IceCube, Phys. Rev. D **89**, 103003 (2014).
[111] V. Pavlidou and B. D. Fields, Diffuse gamma rays from Local Group galaxies, Astrophys. J. **558**, 63 (2001).
[112] D. Gaggero and M. Valli, Impact of cosmic-ray physics on dark matter indirect searches, Adv. High Energy Phys. **2018**, 3010514 (2018).
[113] P. Blasi and E. Amato, Escape of Cosmic Rays from the Galaxy and Effects on the Circumgalactic Medium, Phys. Rev. Lett. **122**, 051101 (2019).
[114] R. Supper, G. Hasinger, W. H. G. Lewin, E. A. Magnier, J. van Paradijs, W. Pietsch, A. M. Read, and J. Trümper, The second ROSAT PSPC survey of M31 and the complete ROSAT PSPC source list, Astron. Astrophys. **373**, 63 (2001).
[115] R. Supper, G. Hasinger, W. Pietsch, J. Truemper, A. Jain, E. A. Magnier, W. H. G. Lewin, and J. van Paradijs, ROSAT PSPC survey of M31, Astron. Astrophys. **317**, 328 (1997).
[116] R. Shirey, R. Soria, K. Borozdin, J. P. Osborne, A. Tiengo, M. Guainazzi, C. Hayter, N. La Palombara, K. Mason, S. Molendi, F. Paerels, W. Pietsch, W. Priedhorsky, A. M. Read, M. G. Watson, and R. G. West, The central region of M31 observed with XMM-Newton: I. Group properties and diffuse emission, Astron. Astrophys. **365**, L195 (2001).

[117] Z. Li and Q. D. Wang, Chandra detection of diffuse hot gas in and around the M31 bulge, Astrophys. J. **668**, L39 (2007).

[118] K. A. G. Olsen, R. D. Blum, A. W. Stephens, T. J. Davidge, P. Massey, S. E. Strom, and F. Rigaut, The star formation histories of the bulge and disk of M31 from resolved stars in the near-infrared, Astron. J. **132**, 271 (2006).

[119] R. P. Saglia, M. Fabricius, R. Bender, M. Montalto, C. H. Lee, A. Riffeser, S. Seitz, L. Morganti, O. Gerhard, and U. Hopp, The old and heavy bulge of M31: I. Kinematics and stellar populations, Astron. Astrophys. **509**, A61 (2010).

[120] H. Dong, K. Olsen, T. Lauer, A. Saha, Z. Li, R. García-Benito, and R. Schödel, The star formation history in the M31 bulge, Mon. Not. R. Astron. Soc. **478**, 5379 (2018).